Journal of Solid State Chemistry **149,** 226–235 (2000)
doi:10.1006/jssc.1999.8508, available online at http://www.idealibrary.com on IDEAL®

Order–Disorder Phenomena in the Perovskite-Related Oxyborocarbonates $SrMn_{1-y}(B, C)_yO_{3-\delta}$

M. Hervieu, C. Michel, D. Pelloquin, A. Maignan, and B. Raveau

Laboratoire CRISMAT, UMR 6508 associée au CNRS, ISMRA et Université de Caen 6, Boulevard du Marechal Juin, 14050 Caen Cedex, France

Received June 4, 1999; in revised form September 8, 1999; accepted September 21, 1999

The electron diffraction and high-resolution electron microscopy investigation of the oxyborocarbonate $SrMn_{1-y}(C, B)_yO_{3-\delta}$ shows that the carbonate and borate groups substitute for the MnO_6 octahedra in the perovskite matrix, according to a mechanism based on the intergrowth and microtwinning of two basic mother structures, $Sr_5Mn_4CO_3O_{10}$ (S_5M_4C) and $Sr_4Mn_3BO_3O_7$ (S_4M_3B). The two structures, S_5M_4C and S_4M_3B, coexist in the same matrix in the form of intergrowths, whose coherent boundaries are parallel to the $\{210\}_P$ planes of the perovskite structure. It results in the formation of $\{210\}_P$ antiphase boundaries and diamond-shaped domains are formed by combining twinning and intergrowth phenomena. These structural phenomena are compared to the microdomain and concentration wave models observed in alloys. These oxides are antiferromagnetic with $T_N = 250$ K, but weak ferromagnetic couplings are detected below 100 K.

INTRODUCTION

The great flexibility of the octahedral framework of the perovskite has allowed a huge number of new frameworks with specific physical properties to be generated, leading for instance to high T_c superconducting (HT_cS) cuprates or to colossal magnetoresistance (CMR) manganites. Among the various mechanisms which lead to new derivatives of the perovskite, the substitution of anionic species for MO_6 octahedra offers a great potentiality. This is the case of the copper oxycarbonates $(Y_{1-x}Ca_x)_nA_{2n}Cu_{3n-1}CO_3O_{7n-3}$ with A = Ba, Sr (1–7), $Sr_2CuO_2CO_3$ (S_2CC) (8), and "S_2CC-2201" or "S_2CC-1201" intergrowths (9–29). In these materials, the introduction of CO_3 groups either generates or destroys superconductivity, depending on their content and arrangement in the structure, i.e., the way they could modify the charge balance and integrity of the copper $[CuO_2]_\infty$ planes.

The possibility to follow a similar route was also observed in the manganites, with the synthesis of the $Sr_5Mn_4CO_3O_{10}$ (30) and $Sr_4Mn_3(B_{1-x}Mn_x)O_{10}$ (31) perovskite derivatives. The two structures are built up by replacing, in an ordered way, some of the MnO_6 octahedra by carbonate and borate groups, respectively. This ordered replacement leads to the formation of tunnels, bordered by MnO_5 pyramids and occupied by the triangular groups. In $Sr_5Mn_4CO_3O_{10}$ (30) (Fig. 1a), one octahedron out of five is replaced, so that a Mn_4O_{10} framework of corner-sharing MnO_5 pyramids is formed which exhibits tunnels occupied by the carbonate groups. The tetragonal cell parameters are $a = a_p \times \sqrt{5}$ and $c = a_p$. In $Sr_4Mn_3BO_3O_7$ (31) (Fig. 1b), one octahedron out of four is replaced; the structure framework is also formed of corner-sharing MnO_5 pyramids and exhibits tunnels occupied by the borate groups. The cell is orthorhombic with $a = a_p$, $b = 4a_p$, and $c = 2a_p$. In spite of their different compositions, and of their complex crystal chemistry, these two compounds exhibit similar magnetic properties: they are both antiferromagnets with T_N value of 260 and 240 K, respectively. The close relationships between $Sr_5Mn_4CO_3O_{10}$ (abbreviated S_5M_4C) and $Sr_4Mn_3BO_3O_7$ (abbreviated S_4M_3B) structures suggest that both types should be able to coexist within the same matrix. We have thus investigated, using electron diffraction and high-resolution electron microscopy, the possibility to introduce together the two types of XO_3 groups in the perovskite framework. The present paper shows that a phasoid $SrMn_{1-y}(C, B)_yO_{3-\delta}$ is actually synthesized. In the oxyborocarbonates, the two structures, S_5M_4C and S_4M_3B, are intergrown in the plane perpendicular to their tunnel axis, forming antiphase boundaries parallel to the $\{210\}_P$ plane of the perovskite structure. Two successive mixed Mn/C (or Mn/B) layers perpendicular to the tunnel axis can also be shifted with respect to each other. All these mechanisms generate the formation of coherent domains, whose widths range between a few angstroms to a few hundred nanometers. The role of twinning in the formation of phasoïds is also evidenced.

EXPERIMENTAL

The system Sr–Mn–C–B–O was investigated according to the generic formula $Sr_4(Mn_{3+x}B_{0.5}C_{0.5-x})O_{10.25-0.5x}$.

0022-4596/00 $35.00

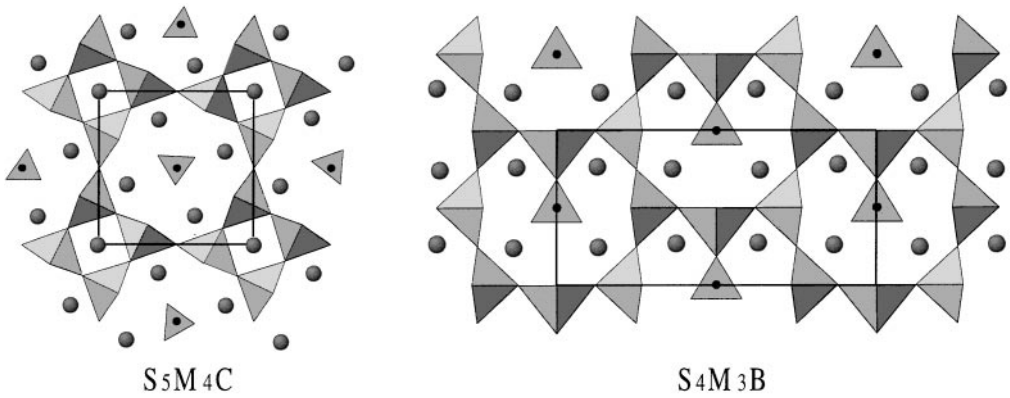

FIG. 1. Idealized drawing of the (a) $Sr_5Mn_4CO_3O_{10}$ structure (denoted S_5M_4C) and (b) $Sr_4Mn_3BO_{10}$ structure (denoted S_4M_3B).

The samples were prepared, by solid state reaction, thoroughly mixing $\frac{1}{16}B_2O_3$ and $1SrO_2$ (note that this precursor is well-known to be carbonated, and therefore no carbonate source was added), with appropriate amounts of Mn_2O_3/Mn so that the ratio $Mn/B = 2(3 + x)$ and the oxidation state of Mn kept close to $+3$; x was varied from 0 to 0.5. The mixtures were introduced in a sealed evacuated silica tube and then heated up to a temperature close to 1000°C, at 150°C h^{-1}, kept at this temperature for 24 h, and quenched to room temperature.

The electron diffraction (E.D.) study was carried out using a JEOL 200 CX microscope fitted with an eucentric goniometer ($\pm 60°$) and high resolution electron microscopy (HREM) with a TOPCON 02B microscope (200 kV and $C_s = 0.4$ mm). Both microscopes are equipped with KEVEX energy dispersive spectroscopy (EDS) analysers.

HREM image simulations were calculated, along the different crystallographic axes of the two S_5M_4C and S_4M_3B structures (presented in Fig. 1), using the Mac-Tempas multislice program. We used the positional parameters of the two mother structures, refined from XRD and ND data (30–31). The through focus series were calculated for different crystal thicknesses. For the images (see HREM section) were the heavy electron density zones (Sr and Mn positions) are highlighted, the C and B atoms appear as grayer dots. Another interesting contrast is the one where these light atom positions appear as very bright spots, since it gives rise to easily interpretable images. In the S_5M_4C-type structure, the bright dots are arranged in a (8.8×8.8)-Å^2 square array (see C positions in Fig. 1a). In the S_4M_3B-type structure, they are arranged in a centered rectangular way, giving rises to a pseudohexagonal array of the bright dots (see B positions in Fig. 1b).

X-ray powder diffraction (XRPD) patterns were collected using a Philips vertical diffractometer equipped with a secondary graphite monochromator and working with the Cu$K\alpha$ radiation. Data were collected by step scanning over the angular range $5° \leq 2\theta \leq 100°$.

The susceptibility was deduced from magnetization measurements collected with a Quantum Design SQUID magnetometer ($5 \leq T \leq 400$ K) under the same applied field of 3 kG. AC susceptibility was also measured in a small H_{ac} magnetic field of 10 Oe with a Lake Shore susceptometer.

RESULTS AND DISCUSSION

For the $x \approx 0.2$–0.3 compounds, the XRPD analyses evidence the formation of perovskite-related compounds, whose patterns are closely related to the $Sr_5Mn_4CO_3O_{10}$ (30) and $Sr_4Mn_3BO_3O_7$ (31) ones. One typical example, recorded for a compound of nominal composition $x = 0.2$, is given in Fig. 2. Note that weak diffraction peaks (labeled C and B) are observed at low angles which could suggest a mixture of S_5M_4C and Sr_4M_3B has been obtained. In fact, as it will be further shown, all the grains are made of coherent S_5M_4C and S_4M_3B domains, which give rise to observable peaks as soon as the diffracting volume of the domain is large enough. Considering a perovskite subcell (a_p), the orthorhombic cell parameters have been refined from XRPD data, to

$$a = 3.9457(5)\ \text{Å},\ b = 3.8673(4)\ \text{Å},\ \text{and}\ c = 3.7907(5)\ \text{Å}.$$

The c parameter is very close to the ones of the mother structures, namely, 3.7848(1) Å for S_5M_4C and 3.7865(1) Å for S_4M_3B. The cell volume, 57.939 Å^3, is intermediate between the ones of the two mother subcells, 58.54 Å^3 for S_5M_4C and 57.435 Å^3 for S_4M_3B. Due to the complex microstructures, characterized by TEM, no attempt for accurate structure refinement has been carried out.

The EDS analyses show that the average Sr/Mn ratio of the grains is rather constant, i.e., close to 5/4 for the $x = 0.2$ sample. It is of course impossible to determine B and C

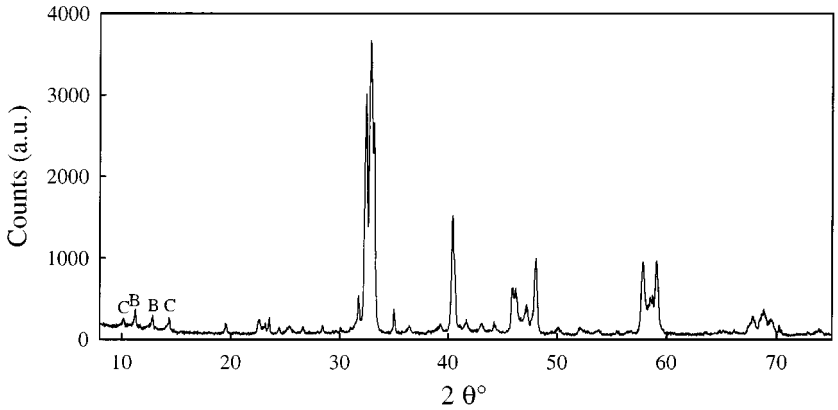

FIG. 2. Typical XRPD pattern of the oxyborocarbonates ($x = 0.2$).

content by EDS analyses, but considering the experimental Sr/Mn content is 5/4 and the nominal Sr/B ratio is 8, the composition would be close to $Sr_4Mn_{3,2}B_{0.5}C_{0.3}O_{10.15}$.

Electron Diffraction

The selected area electron diffraction (SAED) patterns reflect the high complexity of the as-synthesized oxycarbonoborates. All these patterns are characterized by a similar system of intense Bragg reflections which is that of the perovskite subcell (Figs. 3a, 3b, and 4) but, in all them, there is at least another system of weak and/or diffuse additional spots. In fact, there is no archetype, but all the patterns can be interpreted on the basis of the coexistence of only two basic perovskite-related superstructures, namely, the S_5M_4C and S_4M_3B types. They show that all the possible different variants (orientations and translations) of the two mother structures are systematically accommodated within the grains, adopting the different states between the short-range ordering (SRO) and the long-range ordering (LRO).

Different examples are shown in Figs. 3a, 3b, and 4, which illustrate the most typical looks of these patterns and the correlated microstructural features:

— The first pattern in Fig. 3a is mainly generated by the superposition of 90° oriented domains in S_4M_3B, and that of Fig. 3b by 127° oriented domains in S_5M_4C. These twinning domains result from the ordering of the Mn/B and Mn/C atoms along the equivalent $[100]_P$ and $[210]_P$ directions of the perovskite subcell, respectively. These features have been previously reported in the S_4M_3B and S_5M_4C crystals (30–32).

— In Fig. 4a, the intense reflections are characteristic of the S_4M_3B ordering but one observes two types of additional phenomena: streaks along $[210]^*_P$ (equivalent to [011]* of the S_4M_3B cell) and weak reflections in incommensurate positions (several satellites are indicated by small white arrows). The directions of the streaks are indicated by dotted lines. The streaky lines are associated with the existence of defective slices stacked along that direction. In the present pattern, only the first-order satellites are observed along the b^* axis. Similar satellites have been also detected in S_4M_3B (31). In this paper, the ED pattern of a modulated area with $q^* = 0.57c^*$ ($0.57 \approx 4/7$) was given as an example. These satellites are generated by the formation of local intergrowths which will be discussed further.

— In Fig. 4b, the aforementioned features exist but another extra system of diffuse streaky lines is observed; the diffuse lines are parallel to the a^* and b^* axes of the S_5M_4C system. The two systems are pointed out by dotted lines.

— In the last example, Fig. 4c, the reflections of the perovskite subcell are intense with regard to the very weak superstructure reflections. In Fig. 4c, the weak reflections are those of the S_5M_4C system, which develops diffuse wings toward the S_4M_3B spot positions. The opposite system, namely, the S_4M_3B system which develops diffuse wings toward the S_5M_4C positions, is also observed.

All these phenomena suggest the existence of complex microstructures correlated to different stacking modes of defective slices and the formation of coaxial microdomains, which have been examined by HREM.

High-Resolution Electron Microscopy

The $[001]_P$ high-resolution image given in Fig. 3c presents a typical example of adjacent S_5M_4C and S_4M_3B coaxial domains. The focus value is assumed to be close to −55 nm; i.e., the heavy electron density zones (Sr and Mn positions) are highlighted. The contrast observed in each of the domains is similar to the ones previously reported for S_4M_3B (31) and S_5M_4C (30). The through focus series confirm that the Mn and X (C or B) atoms are ordered according to the S_4M_3B- and S_5M_4C-type structures, in agreement with the theoretical images calculated for various focus values and crystal thicknesses for the two structures.

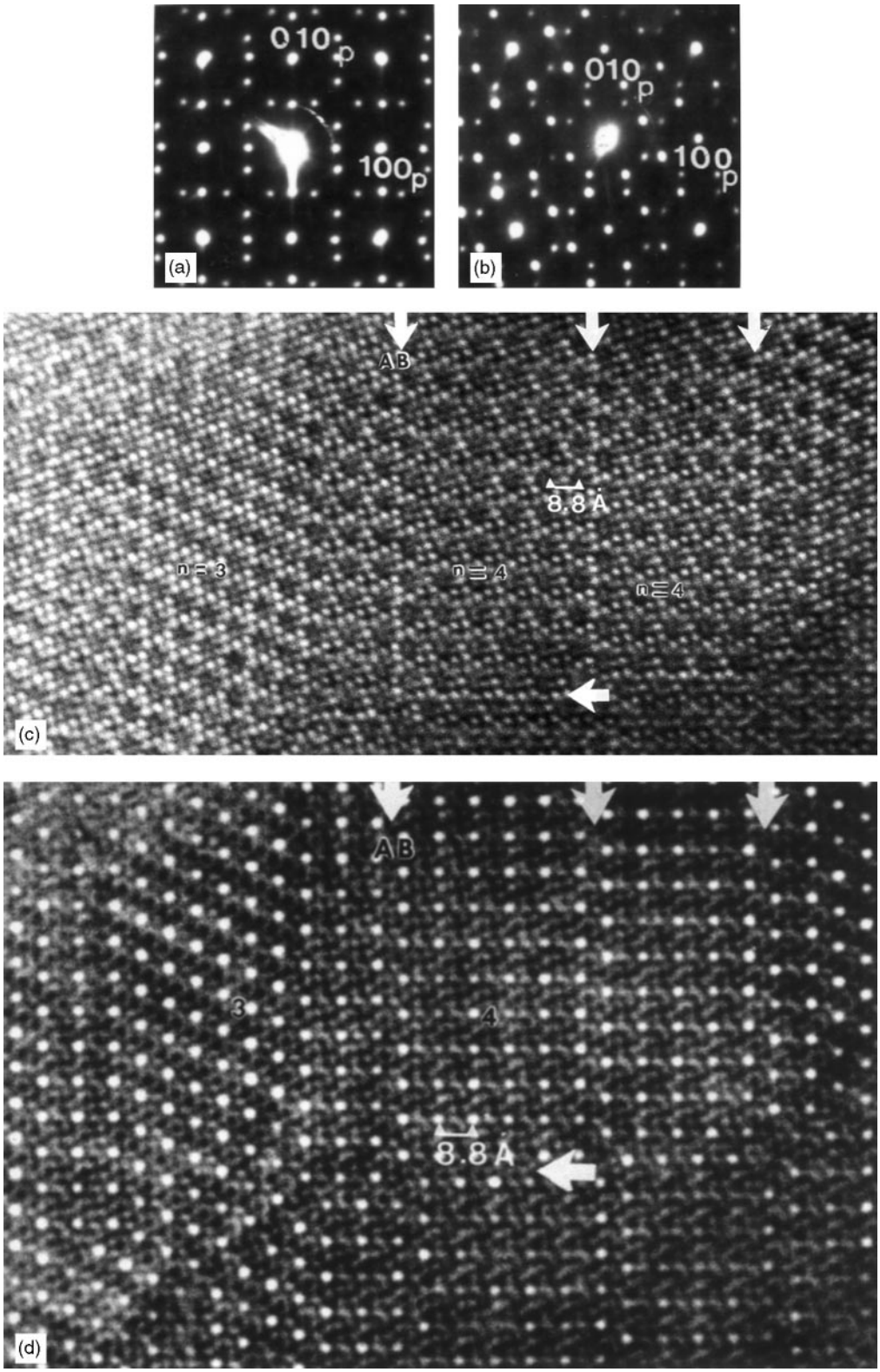

FIG. 3. Twinning domains generated by the ordering of the Mn/B and Mn/C atoms along the equivalent $[100]_P$ and $[210]_P$ directions of the perovskite subcell: (a) ED patterns of 90° oriented domains in S_4M_3B, (b) ED patterns of 127° oriented domains in S_5M_4C, and [001] HREM images of S_5M_4C and S_4M_3B coaxial domains, (c) the heavy electron density zones are highlighted whereas in (d) the tunnel positions (occupied by B or C) appear as very bright spots. The antiphase boundaries (ABs), indicated by large white arrows, correspond to an $n = 3$ S_4M_3B single member in an $n = 4$ S_5M_4C matrix, perpendicular boundaries can be observed.

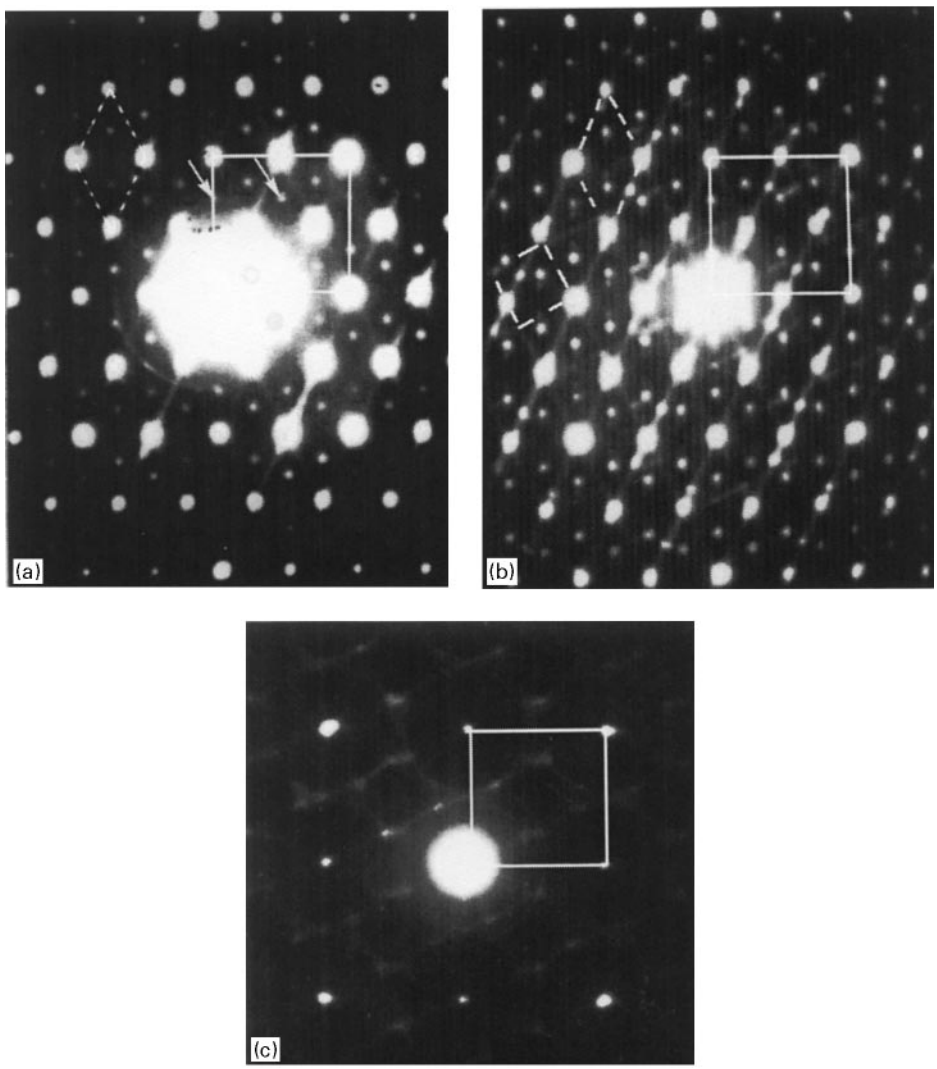

FIG. 4. Examples of ED patterns showing the different systems of reflections (the common perovskite subcell is indicated by white lines): (a) Intense system of S_5M_4C and streaks along $[210]^*_P$ and satellites (small arrows) in incommensurate positions ($q^* = 0.57^*_c$). (b) Intense system of S_4M_3B and diffuse streaky lines parallel to the a^* and b^* axes of the S_5M_4C system. (c) Intense reflections of the perovskite subcell and weak reflections of the S_5M_4C system in the form of diffuse wings toward the S_4M_3B spot positions.

The contrast for which the light atom positions (B or C), i.e., the tunnel positions, appear as very bright spots give rise to $[001]_P$ images easily and directly interpretable (Fig. 3d). In the S_5M_4C-type domains one observes a square array of very bright dots, 8.8 Å on each side, which is correlated to the arrangement of the CO_3 groups in the perovskite matrix (idealized drawing in Fig. 5a). In the S_4M_3B-type domains a diamond-shaped array of bright dots is obtained, 8.8 Å on each side and 53° vertex angle, which is correlated to the distribution of the BO_3 groups (idealized drawing in Fig. 5b). These two geometrical, square and diamond shape, arrays allow the XO_3 groups arrangements, namely, the S_5M_4C- and S_4M_3B-type structures, to be easily identified and distinguished. Comparing Fig. 3c and Fig. 3d, recorded for exactly the same area, provides a good understanding of the main structural features of the two perovskite-related frameworks: the Sr and Mn positions for a focus values of ≈ -55 nm and the C or B positions for the focus value ≈ -30 nm, respectively. The most remarkable feature of the two arrays deals with the fact that they exhibit an identical arrangement of the C (or B) and Mn atoms along a single direction, $[210]_P$, of the perovskite subcell (compare Figs. 5a, 5b). The periodicity along the direction is $a_p\sqrt{5}$. As a consequence, two adjacent S_5M_4C and S_4M_3B domains (Figs. 3c, 3d) can exhibit a coherent boundary (denoted B in Fig. 5c), parallel to the $\{210\}_P$ planes of the perovskite subcell, i.e., to $(100)_{S_5M_4C}$ or to $(110)_{S_4M_3B}$. The great adaptability of these two structures through the $\{210\}_P$ planes is

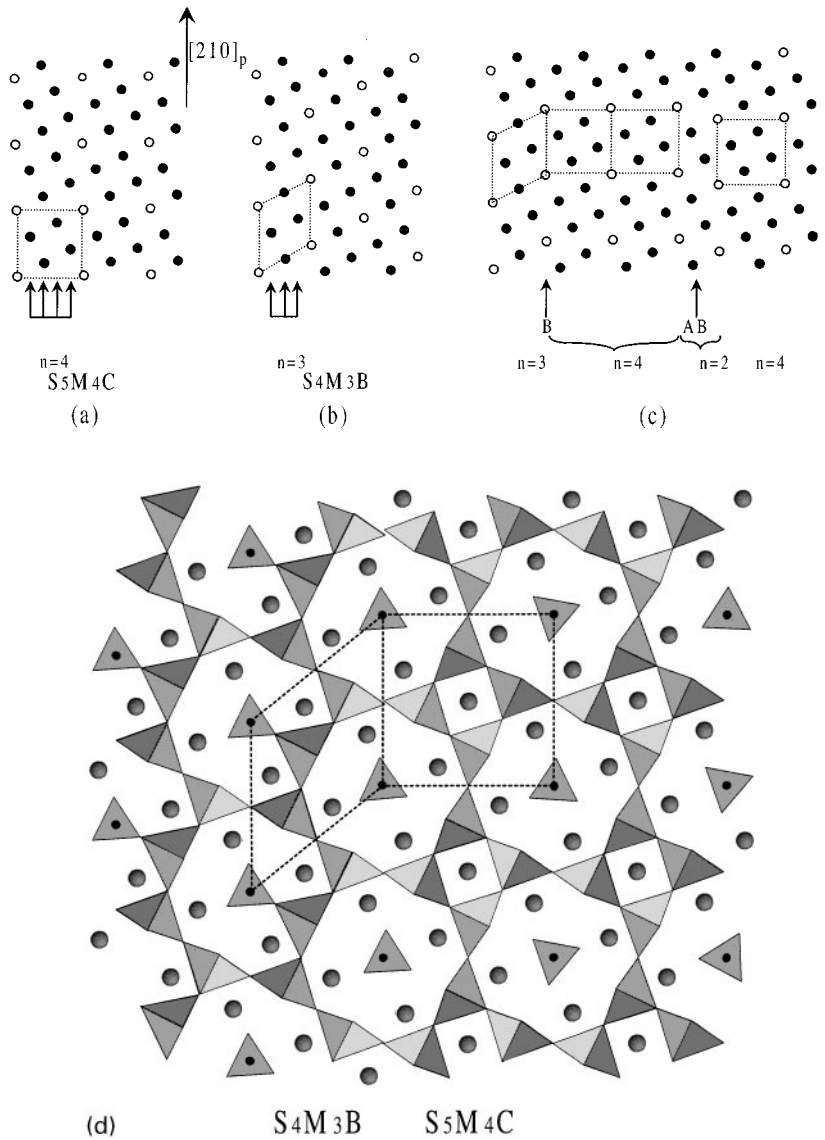

FIG. 5. Idealized representation of the Mn (black circles) and X (open circles) distribution in (a) S_5M_4C structure, (b) S_4M_3B structure, and (c) antiphase boundaries through $n = 2$ or $n = 3$ members within the $n = 4$ matrix (S_5M_4C structure). (d) Drawing of the $n = 3/n = 4$ boundary, taking the polyhedra into consideration.

better shown in Fig. 5d by drawing MnO_6 and CO_3 (or BO_3) polyhedra.

The existence for such $\{210\}_P$ boundaries between the S_5M_4C and S_4M_3B structures leads us to propose another description of the perovskite-related structures of these two compounds, based on the stacking of $\{210\}_P$ pure octahedral manganese layer with $\{210\}_P$ pure carbonate or borate layers. In this description, the S_5M_4C structure consists of the stacking along $[100]_{S_5M_4C}$ of one carbonate layer C with a quadruple manganese layer alternately (Fig. 5a), whereas the S_4M_3B structure is built up from the stacking along $[1\bar{1}0]_{S_4M_3B}$ of one borate layer with a triple Mn layer, alternately (Fig. 5b). It is then obvious that the thickness of the "Mn" layers, i.e., the number n of adjacent Mn layers between two successive B or C layers, can be varied, giving rise to a large series of compounds with the generic formula $Sr_{n+1}Mn_n(XO_3)O_{3n-2}$ (with $X = B$, C). In keeping with this formulation, S_5M_4C and S_4M_3B represent the $n = 4$ and $n = 3$ members, respectively.

Based on this mechanism, ordered or disordered intergrowths of different n members and susceptible to appearing within the same crystal. A first example can be seen in

Fig. 3d where two $n = 4$ members are separated by antiphase boundaries (ABs), indicated by large white arrows. In fact, such antiphase boundaries correspond to the local appearance of a slice of a defective member, $n = 2$ or $n = 3$, within the $n = 4$ matrix (Fig. 5c). In other words, the antiphase boundary results from the formation of disordered intergrowths in the regular $n = 4$ matrix.

Actually, the microstructure of these oxyborocarbonates is, most of the time, more complex than described above. An example is given in Fig. 6, where one observes a S_4M_3B area ($n = 3$), with numerous diamond-shaped domains separated

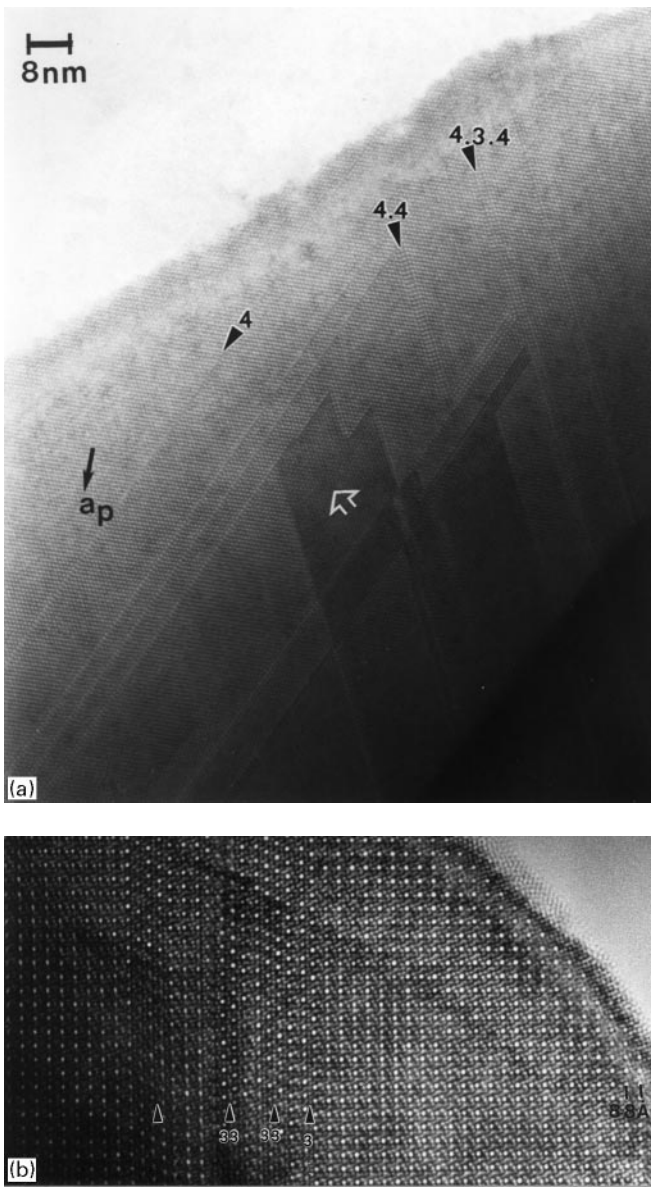

FIG. 6. (a) HREM image of diamond-shaped S_4M_3B domains. The ABs are labeled considering the member formed at the junction. (b) In S_5M_4C, the ABs are made of S_4M_3B defective members.

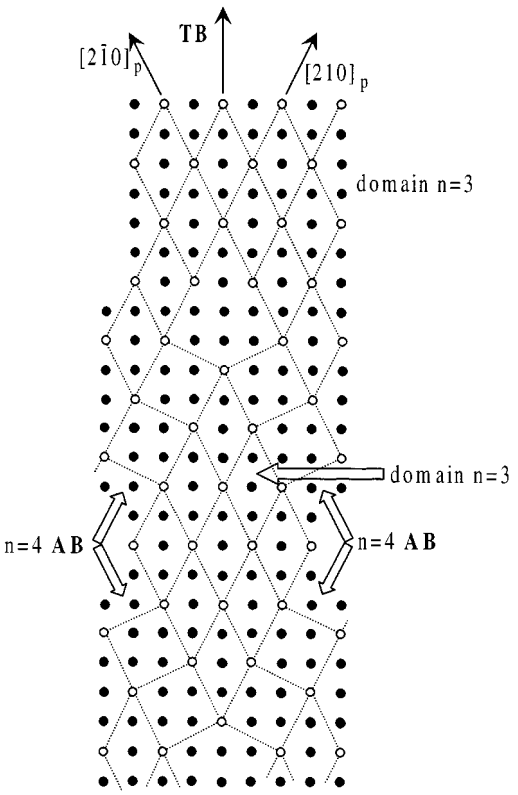

FIG. 7. Idealized drawing of twinning mechanisms.

by ABs indicated by small black arrows. In this area, the ABs correspond to the local formation of $n = 2$ or $n = 4$ intergrowth defects. For instance, the AB labeled "**4**" corresponds to the local formation of one $n = 4$ member in the $n = 3$ matrix whereas the one labeled "**4.4**" consists of two adjacent $n = 4$ members. Thicker ABs corresponding to a more complex sequence are observed, as shown for the one labeled "**4.3.4**", which is a local intergrowth of the $n = 3$ and $n = 4$ members. One remarkable feature concerns the fact that the antiphase boundaries draw broken lines with a constant angle close to 53°, leading to diamond-shaped domains. This geometry is directly linked to that of the orthorhombic S_4M_3B cell, which could be described from a smaller monoclinic cell (Fig. 5d), whose β angle therefore appears as a constant structural parameter. It results from the fact that the $\{210\}_P$ plane is common to the two structures S_4M_3B and S_5M_4C so that the S_5M_4C structure can form a zigzag AB between two S_4M_3B domains, based on a twinning mechanism as described in Fig. 7. In fact, the twinning boundary (TB) is parallel to $\{100\}_P$ so that the angle remains constant, whatever the inner nature of the AB, i.e., whatever n. Very similar, but reversed, phenomena are observed in the $n = 4$ area where $n = 3$ intergrowth defects form ABs. In Fig. 3c, single $n = 3$ members are only observed, indicated by large white arrows. In Fig. 6b, one

observes one single and two double $n = 3$ defective members, indicated by "**3**" and "**3**", respectively, but there are also four adjacent $n = 3$ defective members (unlabeled triangle).

Consequently, when the distance between adjacent ABs decreases, the notion itself of AB can even be replaced by the notion of disordered intergrowths, and when the number of adjacent defective members increases, this notion is replaced by the formation of coaxial domains. The former point is illustrated in Fig. 8, where several (black numbers) of the $n = 3$ adjacent members that are separated by a single $n = 4$ member (black arrow) form a polytype-rich area.

Besides the diamond-shaped and rectangular domains, the HREM images show that there sometimes exist more complex translations. Contrary to the aforementioned ones, these mechanisms imply a [*hkl*] translation vector with $l \neq 0$, i.e., which does not lie in (001) where the superstructures takes place. This can be easily observed in Fig. 6a, where the positions of the columns of B atoms along the viewing direction appear as very bright spots. However, in a few domains, as the one indicated by a white arrow, the brightness of these spots is considerably weaker. Such a contrast suggests that the composition of the columns along *c* is modified. This different contrast can, for example, be explained by the superimposition of $[100]_-$ and $[001]_-$ oriented S_4M_3B domains. Similar contrast variations, generated by similar features, are also observed in the S_5M_4C domains (open white arrow in Fig. 9a).

These results show that there is no real difference between the nature of the domains and ABs, which only differ by their width. The numerous possibilities of the respective orientations of the domains and their highly variable widths explain the variation of SAED patterns from one crystal to the other, from rather intense superstructure spots to diffuse wings (Figs. 3a, 3b, and 4). The incredible richness of the multiple domains is illustrated in Fig. 9. Fig. 9a is an example of the formation of a mosaic structure of S_4M_3B- and S_5M_4C-type areas, each of them being broken by numerous ABs. The width of the two types of domains range from a few to a few tens of nanometers. In Fig. 9b, the mosaic structure is built up from nanodomains at the limit level of a single unit. Note that the formation of 127° twinned domains in S_5M_4C, which only results from C and Mn ordering within an undisturbed perovskite framework, necessarily involves the local formation of, at least, a different C/Mn arrangement (Fig. 5c), favoring the mosaic structures. One example is given in Fig. 9c where the junction area of four twinned S_5M_4C domains (see black arrows) draws a hexagonal arrangement of the carbonate/borate groups (see the black star).

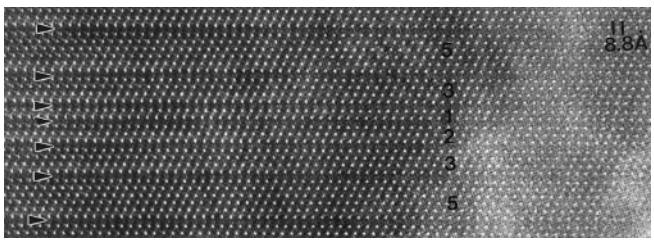

FIG. 8. Intergrowth of $n = 3$ adjacent members with one single $n = 4$ member, leading to complex polytypes.

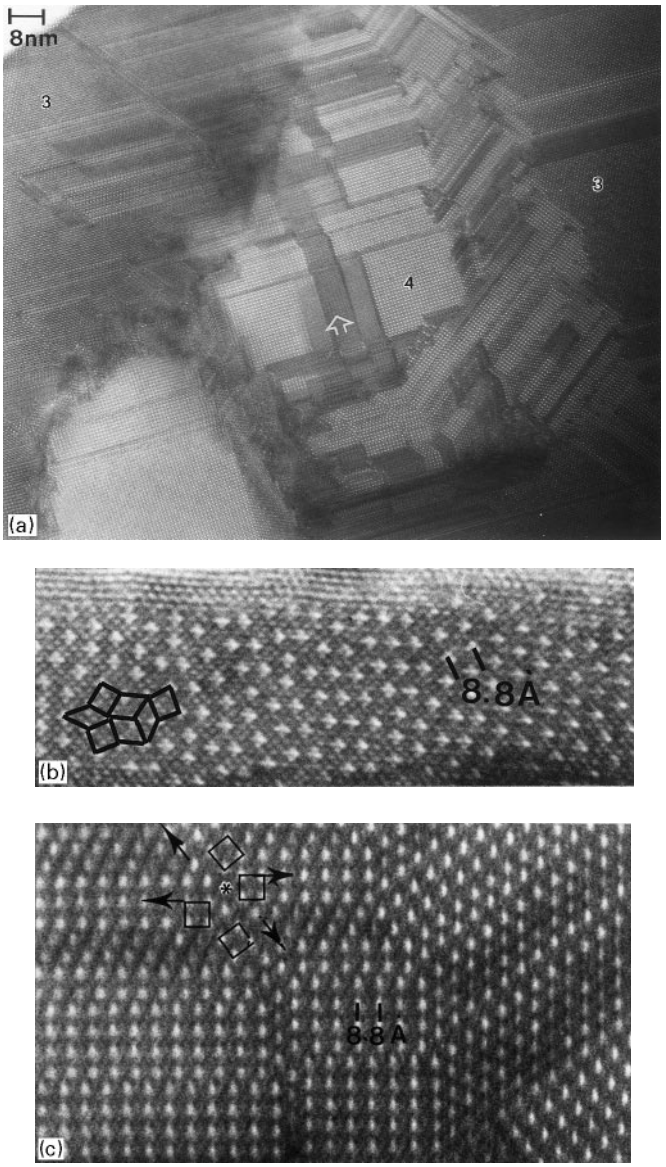

FIG. 9. The domain sizes are highly variable: (a) domains in mosaic structure and (b) "single" cell domains of a phasoid with a Penrose-like arrangement of lozenges and squares. (c) Four twinned S_5M_4C domain junctions.

These images show that the C/B/Mn ordering *is sometimes only* established over a short range and forms a mosaic which is a "Penrose"-like cobbling of the plane. Note

that, in these phasoïds and mosaic structures, every variant of the mother structures appear but the coherence along the third direction is mainly retained.

Magnetic Behavior

The $\chi^{-1}(T)$ curve (Fig. 10) reveals antiferromagnetic behaviour with T_N close to 250 K. This value and the shape of the curve are very similar to the $\chi^{-1}(T)$ already reported for the oxycarbonate $Sr_5Mn_4CO_3O_{10}$ (30) and oxyborate $Sr_4Mn_3(B_{1-x}Mn_x)O_{10}$ (31) which exhibit T_N values of 240 and 260 K, respectively.

Apart from the change of slope at T_N, χ^{-1} strongly decreases below 100 K, suggesting the occurrence of a ferromagnetic coupling. However, the field-dependent magnetization curve, registered at 10 K, does not show any hysteresis (Fig. 11), which would be characterized by a difference between the ascending and descending field branches (labeled 1 and 2 on the graph) and a tendency toward saturation. Moreover, the magnetization value in 50 kG reaches only 0.31 μ_B for three Mn sites, which remains far below the maximum value of 12 μ_B. The slope of the M(H) curve is slightly bent, which is consistent with a weak ferromagnetism, the structures of the carbonates, borates, and oxyborocarbonates, limiting any kind of long-range ferromagnetic ordering.

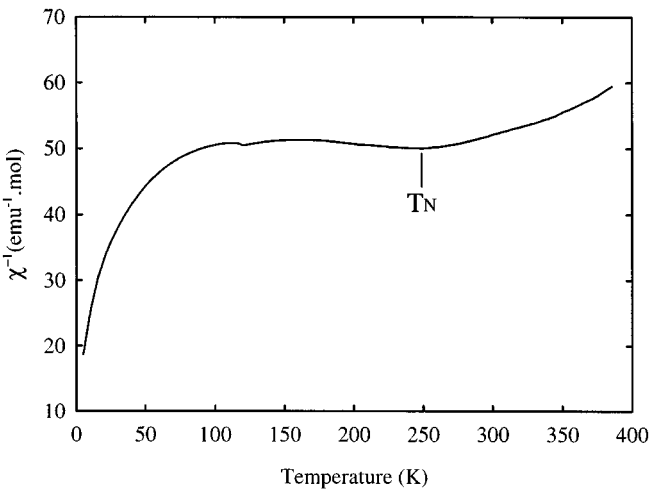

FIG. 10. $\chi^{-1}(T)$ curve characteristic of antiferromagnetic behavior with T_N close to 250 K.

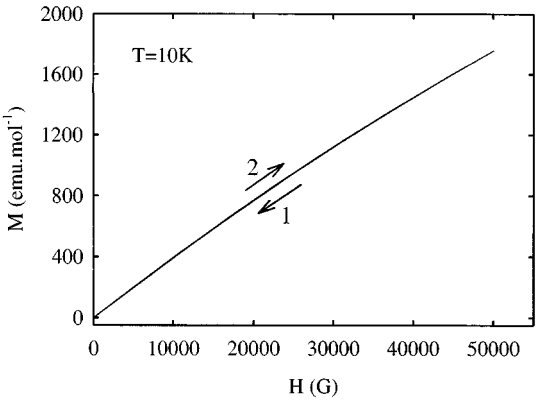

FIG. 11. Field-dependent magnetization curve, registered at 10 K.

CONCLUDING REMARKS

Order–disorder phenomena are commonly observed in perovskite-related compounds, according to a large variety of mechanisms. The nature of the ones established in this oxyborocarbonate can be compared to those observed in the 1201-type cuprates $Tl_{1-x}M_xSr_2CuO_5$ (33), with M = Ta, Nb, and W, and the rock salt-type TiO_x (34) in which the ordering modes are similar to that adopted by binary alloys. One can indeed compare these phenomena with the long-range ordering (LRO) and short-range ordering (SRO) observed in the so-called $D1_a$ and DO_{22} structures (35–37). The introduction of a slab of $D1_a$ configuration (superstructures along the equivalent {210} and square configuration as in S_5M_4C) causes a shift of 1/4 of the (101) planes and of 1/2 of the (202) planes in the DO_{22} structure (superstructures along the equivalent {100} and lozenge configuration as in S_4M_3B). Van Tendeloo and colleagues present two different descriptions of the short-range ordering (SRO), a "microdomain" model and a "concentration wave" model considering atomic planes built up from similar atomic rows (compare to Fig. 5) and discuss the order–disorder in terms of metallic clusters. They also test the proposed models by constructing optical gratings representing the projected atomic configurations (37). The optical diffraction patterns and the diffuse intensity contours they obtained present striking similarities with those recorded in the present oxides (Figs. 3a, 3b, and 4). However, we must indeed keep in mind that the present ordering is not simply observed in a binary compound but in a complex quaternary system and that the ordering features occur between MnO_5 pyramids and XO_3 triangular groups, within a complex framework including also the strontium cations.

Finally, it is remarkable that the $\{210\}_P$ planes which form these structures are built up from ribbons of corner-sharing pyramids which are three-pyramids-wide in S_4M_3B and four-pyramids-wide in S_5M_4C. Such a topology, involving four-pyramids-wide ribbons, is also observed in $Sr_2Mn_2O_5$ (38, 39). The close relationships between these structures suggest the possibility of creating new well-ordered oxyborocarbonates, by controlling the synthesis conditions, whose magnetic properties should be investigated.

REFERENCES

1. J. Akimitsu, M. Uheara, M. Ogawa, H. Nakata, K. Tomimoto, Y. Miyazaki, H. Yamane, T. Hirai, K. Kinoshita, and Y. Matsui, *Physica C* **201,** 320 (1992).
2. B. Domenges, M. Hervieu, B. Raveau, *Physica C* **207**(1,2), 65–78 (1993).
3. Ph. Boullay, B. Domenges, M. Hervieu, and B. Raveau, *Chem. Mater.* **5,** 1683–1686 (1993).
4. M. Hervieu, Ph. Boullay, B. Domenges, A. Maignan, and B. Raveau, *J. Solid State Chem.* **105**(1), 300–304 (1993).
5. A. Maignan, M. Hervieu, C. Michel, and B. Raveau, *Physica C* **208**(1,2), 116–120 (1993).
6. M. Hervieu, C. Michel, and B. Raveau, *Chem. Mater.* **5**(8), 1126–1113 (1993).
7. T. Krekels, O. Milat, G. Van Tendeloo, J. Van Landuyt, S. Amelinckx, P. R. Slater, and C. Greaves, *Physica C* **210,** 439 (1993).
8. D. V. Fomichev, A. L. Kharlanov, E. V. Antipov, and L. M. Kouba, *Superconductivity* **3,** 126 (1990).
9. X. F. Zhang, G. Van Tendeloo, S. Amelinckx, D. Pelloquin, C. Michel, M. Hervieu, and B. Raveau, *J. Solid State Chem.* **113**(2), 327 (1994).
10. D. Pelloquin, M. Hervieu, A. Maignan, C. Michel, M. T. Caldes, and B. Raveau, *Physica C* **232**(1,2), 75 (1994).
11. D. Pelloquin, M. T. Caldes, A. Maignan, C. Michel, M. Hervieu, and B. Raveau, *Physica C* **208**(1,2), 121 (1993).
12. H. Uheara, H. Nakata, J. Akimitsu, T. Den, T. Kobayashi, and Y. Matsui, *Physica C* **213,** 51 (1993).
13. D. Pelloquin, M. T. Caldes, C. Michel, A. Maignan, M. Hervieu, and B. Raveau, *Physica C* **217**(1,2) 27 (1993).
14. M. Hervieu, M. T. Caldes, D. Pelloquin, C. Michel, S. Cabrera, and B. Raveau, *J. Mater. Chem.* **6**(2), 175 (1996).
15. Y. Matsui, M. Ogawa, H. Uheara, and J. Akimitsu, *Physica C* **217,** 287 (1993).
16. D. Pelloquin, M. Hervieu, C. Michel, A. Maignan, and B. Raveau, *Physica C* **227,** 215 (1994).
17. D. Pelloquin, M. Hervieu, S. Malo, C. Michel, A. Maignan, and B. Raveau, *Physica C* **246,** 1 (1995).
18. A. Maignan, D. Pelloquin, S. Malo, C. Michel, M. Hervieu, and B. Raveau, *Physica C* **249,** 220 (1995).
19. M. Huve, G. Van Tendeloo, S. Amelinckx, M. Hervieu, and B. Raveau, *J. Solid State Chem.* **120,** 332 (1995).
20. M. Uheara, S. Sahoda, H. Nakata, J. Akimitsu, and Y. Matsui, *Physica C* **222,** 27 (1994).
21. M. Kikuchi, E. Oshima, N. Ohnishi, Y. Muraoka, S. Nakajima, M. Aoyagi, E. Ogawa, J. Akimitsu, T. Oku, K. Hiraga, and Y. Syono, *Physica C* **219,** 200 (1994).
22. T. Noda, M. Ogawa, J. Akimitsu, M. Kikuchi, E. Ohshima, and Y. Syono, *Physica C* **242,** 12 (1995).
23. S. Malo, D. Pelloquin, A. Maignan, C. Michel, M. Hervieu, and B. Raveau, *Physica C* **267,** 1 (1996).
24. M. Hervieu, D. Pelloquin, S. Malo, C. Michel, and B. Raveau, *J. Solid State Chem.* **126,** 271 (1996).
25. M. Uheara, H. Nakata, J. Akimitsu, *Physica C* **216,** 453 (1993).
26. M. Uheara, H. Nakata, J. Akimitsu, T. Den, T. Kobayashi, and Y. Matsui, *Physica C* **213,** 51 (1993).
27. M. Huve, G. Van Tendeloo, M. Hervieu, A. Maignan and B. Raveau, *Physica C* **231,** 15 (1994).
28. F. Letouze, C. Martin, A. Maignan, C. Michel, M. Hervieu, and B. Raveau, *Physica C* **254,** 33 (1995).
29. M. Huve, G. Van Tendeloo, S. Amelinckx, M. Hervieu, and B. Raveau, *J. of Solid State Chem.* **120,** 332 (1995).
30. V. Caignaert, B. Domenges, and B. J. Raveau, *J. Solid State Chem.* **120,** 279 (1995).
31. D. Pelloquin, M. Hervieu, C. Michel, N. Nguyen and B. Raveau, *J. Solid State Chem.* **134,** 395 (1997).
32. V. Caignaert, M. Hervieu, B. Raveau, and J. M. Greneche, *Chem. Scripta* **27,** 289 (1987).
33. G. Van Tendeloo, P. De Meunalaere, F. Letouzé, C. Martin, M. Hervieu, and B. Raveau, *J. Solid State Chem.* **113,** 132 (1997).
34. D. Watanabe, O. Terasaki, Jostons, and J. R. Castles, "Chemistry of Extended Defects in Non Metallic Oxides" (L. Eyring and O. Keefe, Eds.), p. 238. North Holland, Amsterdam, 1970.
35. G. Van Tendeloo, *Mater. Sci. Eng.* **26,** 209 (1976).
36. G. Van Tendeloo, J. Van Landuyt, and A. Amelinckx, *Electron Microscopy* **1,** 226 (1980).
37. G. Van Tendeloo, A. Amelinckx, and D. de Fontaine, *Acta Crystallogr. B* **41,** 281 (1985).
38. V. Caignaert, N. Nguyen, M. Hervieu, and B. Raveau, *Mater. Res. Bull.* **20,** 479 (1985).
39. V. Caignaert, N. Nguyen, M. Hervieu, and B. Raveau, *J. Solid State Chem.* **62,** 281 (1986).